

# Modeling Free Surface Flows in Part-Filled Rotating Vessels: Vertical and Horizontal Orientations

K.S.Sujatha and M. F. Webster\*

Institute of Non-Newtonian Fluid Mechanics,  
Department of Computer Science,  
University of Wales, Swansea, SA2 8PP, UK.

## Abstract

This paper reports on the numerical simulation of rotating flows with free surfaces, that arises in the food processing industry, namely in dough-kneading. Free surface flow in a rotating cylinder is investigated when a fluid is stirred in a cylindrical shaped vessel with a stirrer attached to the lid. The equations are solved in a three-dimensional cylindrical polar coordinate system. The numerical simulation is based on a Taylor-Galerkin finite element formation, with an arbitrary Lagrangian-Eulerian scheme to accommodate free-surface movement. Peeling and wetting conditions, that depends on stretch-rate, are modeled to get the exact position of the surface. Free-surface profiles are presented for different speeds of rotation and predictions compare closely to equivalent experimental results. This is re-echoed through torque-time traces for the part-filled situations, that demonstrate the distribution of torque and hence the rate-of-work done, in the kneading process.

KEY WORDS: Dough-kneading, non-Newtonian, free-surface, Lagrangian-Eulerian, rotating flows, wetting and peeling.

## 1. Introduction

This paper addresses the numerical simulation of free-surface flows in rotating cylindrical-shaped vessels, that arises in the food processing industry. The motivation for this work is to develop an advanced technology to model dough kneading. The ultimate objective is to provide a predictive capability from which optimal designs for dough mixers may emerge.

Free surface flows are common in everyday experience and some industrial processes. There are several ways of treating moving free-surfaces. These are comprehensively reviewed in ref[1]. The first category comprises methods moving the mesh system itself in a Lagrangian sense, following the movement of the fluid (eg. Marker Particle method [2]). This method introduces complications within fluid dynamics implementations, because in the course of time, the moving mesh system suffers massive distortion which necessitates re-meshing to rebalance the mesh system.

---

\* Author for correspondence

With Eulerian-based methods, the actual position of the points of the free boundary are localised in a fixed mesh. The governing equations are solved in a larger domain that is actually occupied by the fluid, distinguishing between wet and dry regions (eg. Volume of Fluid method (VOF) of Hirt and Nichols [3]). The original VOF method employed a finite difference scheme and was not straightforward to implement for problems involving complicated boundaries. This method was later extended by various investigators to solve a variety of problems, such as mould-filling and metal casting. The VOF method, based on finite element techniques, was also developed but was only applied to solve relatively simple problems, due to the complexities involved [4]. Subsequently, an improved version of the VOF method was developed, in which the flow field is treated as a two-phase system. In this method, the regions filled with fluid are assumed to be within one phase. The dry region, separated by the free surface boundary, is considered as a second phase. It is assumed that the dry regions consist of a virtual fluid, where artificial physical properties are assumed. Thus, this scheme is termed a pseudo-density method [5]. To avoid using artificial physical properties, Nassehi [6] treated the dry section as a compressible fluid. Artificial Lagrangian-Eulerian methods combine the respective advantages of both Lagrangian and Eulerian methods [7]. A mixed Lagrangian-Eulerian method was developed by Ramaswamy [8] for calculating the transient dynamics of incompressible, viscous fluids with free-surfaces.

Sato et al. [9] proposed a fringe element generation method based upon a hybrid finite element/finite volume method. No re-meshing was needed as the fluid flowed over a fixed mesh, wetting new regions. New fringe elements were created in the surface neighbourhood, conforming to the original mesh structure. This approach avoids mesh distortion. Ding et al. [10,11] and Manogg [12] used source propagation and particle tracking methods to model various injection moulding problems. Free-surface flows related to some industrial problems are discussed in references [13,14,15].

In this work, unsteady free-surface flows encountered in dough kneading are modelled. Two different dough mixer designs are investigated. The single rotating stirrer is placed either in a concentric or eccentric arrangement, with respect to the axis of the vessel. As an alternative to conventional mixer operation, the motion is assumed to be driven by the rotation of the vessel, for convenience within the modelling. The first part of this work, dealing with numerical and experimental studies in filled geometries, has been published elsewhere [16, 17, 18, 19]. The mixer is considered in a vertical  $(r, \theta, z)$  and horizontal  $(r, \theta)$  coordinate system orientation, and to be partially filled during the process. This leaves the surface of the fluid to move freely. Special considerations are applied to the free-surface, that is described by a number of particles. The movement of each particle is traced by an Eulerian scheme. In addition, novel strategies are proposed to accommodate for wetting and peeling boundary conditions, that arise at the interface between fluid and solid surfaces.

The simulation employs a Taylor-Galerkin finite element formation for the generalised Navier-Stokes equations. The formation applies a temporal discretisation in a Taylor series, prior to a Galerkin spatial discretisation. A semi-implicit treatment for diffusion is used to address linear stability constraints. The flow is modeled as incompressible via a pressure-correction procedure. An arbitrary Lagrangian-Eulerian scheme is adopted to accommodate free surface movement. A fixed finite element mesh covers the whole domain, that is divided dynamically into two different sections:

one wet and another dry. The position of the free surface defines the fluid region. The solution of the field variables is activated only within the wet fluid zone. The equivalent experimental results presented in this paper involve laser scatter technology and contemporary imaging methods [20, 21]. Similar techniques have been used by Prakash and Kokini [22] to determine velocity vectors associated with flows in model mixers, to ultimately discern shear-rate distribution.

In the kneading process, the quality of the final product (where the internal structure is developed through kneading), depends on the correct balance of mechanical work within the mixer. In the present study, it has proved instructive to construct secondary field data of velocity gradients, local shear-rates and local rate-of-work done. These quantities may be estimated from primary finite element solution field data. Hence, torque and power may be computed, which provide a torque-time trace. Such data aid in the appreciation of effective kneading.

## 2. Basic equations and numerical scheme

For Newtonian and incompressible isothermal flow, the generalized momentum and continuity equations may be expressed as:

$$\rho U_t = \mu \nabla^2 U - \rho U \cdot \nabla U - \nabla P + \rho g \quad , \quad (1)$$

$$\nabla \cdot U = 0 \quad , \quad (2)$$

where variables (U) and pressure (P) are defined over space and time with time derivative represented as ( $U_t$ ). Material properties are given via density ( $\rho$ ) and viscosity ( $\mu$ ).

A Carreau-Yasuda model, represented by equation (1) below, is employed to describe the shear-thinning behavior of the viscosity  $\mu$ ,

$$\mu = \frac{\mu_0 - \mu_\infty}{1 + (\lambda \dot{\gamma})^m} + \mu_\infty \quad , \quad (3)$$

where  $\mu_0$  is a reference viscosity at low shear-rates and  $\mu_\infty$  is an asymptotic value of viscosity at large shear rates;  $\dot{\gamma} = 0.5\sqrt{I_2}$  with the second invariant  $I_2$  of the rate-of-strain tensor,  $m$  is a power law index and  $\lambda$  is a material constant.

For convenience of representation, we adopt non-dimensional variables, via scales as follows:

$$x^* = \frac{x}{L}, \quad u^* = \frac{u}{V}, \quad \mu^* = \frac{\mu}{\mu_c}, \quad t^* = \frac{V}{L} t, \quad P^* = \frac{L}{\mu_c V} P \quad (4)$$

where  $L$ ,  $V$  and  $\mu_c$  are characteristic length, velocity and viscosity respectively. We adopt  $L$  as the diameter of the stirrer,  $V$  the speed of the vessel and  $\mu_c$  a zero shear-rate viscosity (1.05 Pa.s). This leads to a Reynolds number, the non-dimensional group involved, and the coefficient for the gravity term ' $F$ ' defined as:

$$\text{Re} = \frac{\rho L V}{\mu_c}, \quad F = \frac{\rho L^2 g}{\mu_c V} \quad (5)$$

where  $\rho$  is the fluid density. Hereforth, we discard the \* notation for ease of presentation. To be specific, we take  $m = 0.6$  and  $\lambda = 0.083\text{s}$ . Substitution of the above dimensionless variables into equation (1) yields the non-dimensional Navier-Stokes equations,

$$\text{Re}U_t = \nabla^2 U - \text{Re}U \cdot \nabla U - \nabla P + Fg, \quad (6)$$

$$\nabla \cdot U = 0. \quad (7)$$

The algorithm invoked in this study follows references [23, 24, 25]. Briefly, a semi-implicit time-stepping procedure, namely, a Taylor-Galerkin/pressure-correction finite element scheme is employed to solve the governing equations relating to the conservation of mass and momentum. The time-stepping scheme is derived through Taylor series expansions up to second-order in time-step and a two-step predictor-corrector scheme is assumed. This, in conjunction with a second-order pressure-correction method, to accommodate the incompressibility constraint, produces a fractional-staged equation system. This system is solved over three distinct phases within a single time-step. A semi-implicit Crank-Nicolson treatment is adopted in time to discretise the diffusion terms. A Galerkin finite element spatial discretisation renders a fully-discrete system. The choice is made of piecewise continuous quadratics for velocity, and linears for pressure based upon tetrahedral elements in three dimensions (and triangles in two dimensions). Further details on the analysis are published extensively in the literature [23, 24, 25]. The algorithm has three fractional-stages per time-step as follows:

Stage 1: From initial velocity and pressure fields, non-divergence-free  $U^{n+\frac{1}{2}}$  and  $U^*$  fields are calculated via a two-step predictor-corrector procedure. The corresponding equations are solved iteratively by a Jacobi method.

Stage 2: Using  $U^*$ , calculate the pressure difference ( $P^{n+1} - P^n$ ) via a Poisson equation, applying a Choleski method of solution.

Stage 3: Using  $U^*$ , and pressure difference ( $P^{n+1} - P^n$ ), determine the divergence-free velocity field  $U^{n+1}$  by Jacobi iteration.

Adopting quadratic and linear interpolations,  $U(x,t)$  and  $P(x,t)$  may be expressed as:

$$U(x,t) = U_j(t)\phi_j(x), \quad P(x,t) = P_j(t)\psi_j(x)$$

The equation stages in fully-discrete form may be represented in the following form:

stage 1a:

$$\left[\frac{2\text{Re}}{\Delta t}M + \frac{1}{2}S_u\right](U^{n+\frac{1}{2}} - U^n) = \{-[S_u U + \text{Re}N(U)U] + L^T P + F\phi_i g\}^n \quad (8)$$

stage 1b:

$$\left[\frac{\text{Re}}{\Delta t}M + \frac{1}{2}S_u\right](U^* - U^n) = [-S_u U + L^T P + F\phi_i g]^n - \text{Re}[N(U)U]^{n+\frac{1}{2}} \quad (9)$$

stage 2:

$$K(P^{n+1} - P^n) = -\frac{2}{\Delta t} LU^* \quad (10)$$

stage 3:

$$\frac{Re}{\Delta t} M(U^{n+1} - U^*) = \frac{1}{2} L^T (P^{n+1} - P^n) \quad (11)$$

where  $U^n$ ,  $U^{n+1}$ ,  $P^n$  and  $P^{n+1}$  are nodal vectors of velocity and pressure at time  $t^n$  and  $t^{n+1}$  respectively;  $U^*$  is an intermediate nodal velocity vector introduced in step 1b;  $M$ ,  $S_u$ ,  $N(U)$ ,  $K$  and  $L$  are mass matrix, momentum diffusion matrix, convection matrix, pressure stiffness matrix and divergence-pressure gradient matrix, respectively. The above matrices in an  $(r, \theta, z)$  co-ordinate system are defined as:

$$M_{ij} = \int_{\Omega} \phi_i \phi_j d\Omega \quad (12)$$

$$S_u = \begin{bmatrix} S_{11} & S_{12} & S_{13} \\ S_{21} & S_{22} & S_{23} \\ S_{31} & S_{32} & S_{33} \end{bmatrix} \quad (13)$$

$$(S_{11})_{ij} = \int_{\Omega} \left\{ 2 \frac{d\phi_i}{dr} \frac{d\phi_j}{dr} + \frac{1}{r^2} \frac{d\phi_i}{d\theta} \frac{d\phi_j}{d\theta} + \frac{2}{r^2} \phi_i \phi_j + \frac{d\phi_i}{dz} \frac{d\phi_j}{dz} \right\} d\Omega \quad (14)$$

$$(S_{12})_{ij} = (S_{21})^T = \int_{\Omega} \left\{ \frac{2}{r^2} \phi_i \frac{d\phi_j}{d\theta} - \frac{1}{r^2} \frac{d\phi_i}{d\theta} \phi_j + \frac{1}{r} \frac{d\phi_i}{d\theta} \frac{d\phi_j}{dr} \right\} d\Omega \quad (15)$$

$$(S_{13})_{ij} = (S_{31})^T = \int_{\Omega} \left\{ \frac{d\phi_i}{dz} \frac{d\phi_j}{dr} \right\} d\Omega \quad (16)$$

$$(S_{22})_{ij} = \int_{\Omega} \left\{ \frac{2}{r^2} \frac{d\phi_i}{d\theta} \frac{d\phi_j}{d\theta} - \frac{1}{r} \frac{d\phi_i}{dr} \phi_j + \frac{d\phi_i}{dr} \frac{d\phi_j}{dr} + \frac{1}{r^2} \phi_i \phi_j - \frac{1}{r} \frac{d\phi_j}{dr} \phi_i + \frac{d\phi_i}{dz} \frac{d\phi_j}{dz} \right\} d\Omega \quad (17)$$

$$(S_{23})_{ij} = (S_{32})^T = \int_{\Omega} \left\{ \frac{1}{r} \frac{d\phi_i}{dz} \frac{d\phi_j}{d\theta} \right\} d\Omega \quad (18)$$

$$(S_{33})_{ij} = \int_{\Omega} \left\{ \frac{d\phi_i}{dr} \frac{d\phi_j}{dr} + \frac{1}{r^2} \frac{d\phi_i}{d\theta} \frac{d\phi_j}{d\theta} + 2 \frac{d\phi_i}{dz} \frac{d\phi_j}{dz} \right\} d\Omega \quad (19)$$

$$L = (L_1, L_2, L_3) \quad (20)$$

$$L_r = \int_{\Omega} \psi_j \left( \frac{\phi_i}{r} + \frac{\partial \phi_i}{\partial r} \right) d\Omega; L_{\theta} = \int_{\Omega} \psi_j \left( \frac{\partial \phi_i}{\partial \theta} \right) d\Omega; L_z = \int_{\Omega} \psi_j \left( \frac{\partial \phi_i}{\partial z} \right) d\Omega \quad (21)$$

$$N(U)_{ij} = \int_{\Omega} \phi_i \phi_k U_k \nabla \phi_j d\Omega \quad (22)$$

$$(K)_{ij} = \int_{\Omega} \nabla \psi_i \cdot \nabla \psi_j d\Omega \quad (23)$$

where  $d\Omega = r dr d\theta dz$ ; and  $i, j, k = 1, 2, 3$ . After solving for velocities and pressure in the flow field, shear-rate ( $\dot{\gamma}$ ), rate-of-work done ( $\dot{w}$ ) and torque ( $T_q$ ) are computed, using the following relations,

$$\dot{\gamma} = 2\sqrt{II_d} \quad , \quad II_d = \frac{1}{2} \text{trace}(D^2) \quad (24)$$

$$\dot{w}(t) = \int_{\Omega} (\tau : \nabla V) d\Omega = P_w \quad (25)$$

$$(\boldsymbol{\tau} : \nabla \mathbf{V}) = \frac{1}{2} \mu \left( \frac{dV_i}{dX_j} + \frac{dV_j}{dX_i} \right)^2 = \dot{w}(t, x) \quad (26)$$

$$P_w = T_q \omega \quad (27)$$

where ‘D’ is the deformation tensor, ‘ $P_w$ ’ is the power, ‘ $\boldsymbol{\tau}$ ’ is the stress tensor, ‘ $\mathbf{V}$ ’ is the velocity vector, ‘ $\omega$ ’ is the rotational speed of the vessel per second, ‘ $\Omega$ ’ is the fluid volume and ‘ $t$ ’ is the time. Localised rate-of-work done,  $\dot{w}(t, x)$ , may be interpreted as the integrand of equation (25).

The flow problems addressed are specified as follows. The three and two-dimensional geometries are shown in Figs. 1(a-b) and the meshes in Figs. 1(c-f). For the three-dimensional vertical-standing vessel orientation instance, a cylindrical vessel with stirrer (or stirrers) placed in concentric or eccentric orientation with respect to the axis of the vessel are considered. The fluid is driven by the outer-wall and fixed at the top of the vessel by a lid as shown in Fig. 1(a). Here, tetrahedral elements are employed. To create a three-dimensional finite element mesh, first each brick element is formed, which is then subdivided into six tetrahedra. For a single stirrer vessel, Fig. 1(e), this leads to 6000 tetrahedral elements, 9240 velocity nodes and 1320 pressure (vertex) nodes; for the double-stirrer, Fig. 1(f), there are equivalently 8400 tetrahedral elements, 13145 velocity nodes and 1902 pressure nodes. At the start of the simulation, the vessel is sixty percent full. The outer vessel, attached to the bottom plate, rotates at different rotational speeds and the top is held stationary.

For the two-dimensional horizontal-vessel orientation case, the flow geometry is discretised into a triangular mesh, as in Figs. 1(c), (d). So typically, the flow domain is discretised in Fig. 1(c) into 240 triangular elements, 520 velocity nodes and 140 pressure nodes; likewise, for two-stirrers of Fig. 1 (d), discretisation leads to 560 triangular elements, 1195 velocity nodes and 317 pressure nodes.

### 3. Free-surface tracking

An arbitrary Lagrangian-Eulerian method is employed to deal with free surfaces. A fixed finite element mesh applies to the flow domain that is divided dynamically into two distinct parts: one wet and another dry. The position of the free surface defines the fluid region and the domain of solution. The solution of the field variables, such as velocity, pressure and stress, are investigated within the wet fluid zone only. Sub-time steps are introduced to improve the field solution after a shift of the free-surface. So separate time-step control is enforced on the surface movement and for the full wet domain computation. In each Taylor-Galerkin phase, one hundred sub-time steps are performed.

#### 3.1 Particle tracking scheme

Free surface profiles are obtained by tracking particle histories. It is assumed that the fluid surface consists of particles. Their main task is to provide the position so that the configuration of the surface can be determined. For tracking the position, a well-established Runge-Kutta scheme is adopted, which may be represented via an explicit Euler step:

$$x_p^{n+1} = x_p^n + \Delta t v(x_p, t^n) \quad (28)$$

where, for particle  $p$ ,  $x_p^n$  is a position at time  $t^n$ ,  $v(x_p, t^n)$  is a velocity at  $x_p^n$  at time  $t^n$ ,  $x_p^{n+1}$  is a position at time  $t^{n+1}$ . This scheme is performed after stage 3 of each time step of the Taylor-Galerkin algorithm, that is, at the end of each time-step cycle. For practical convenience, a small gap is introduced between the first particle and the cylinder wall to circumvent the indeterminacy of conditions at the free surface-solid wall interface. Typically, between three thousand and six thousand particles are employed to trace the surface.

Particles are introduced on the top of the fluid surface at the start of simulation. The Taylor-Galerkin finite element calculations are performed for the complete domain (wet and dry) to obtain solution (velocities and pressures) at all nodes. The dry and wet regions are distinguished on the basis of material properties (viscosity). If a node is dry, the viscosity is zero and hence the solution is zero. For moving particles, particle velocities  $U(X_p, t^n)$  are calculated by interpolating nodal velocities.

$$U(X_p, t^n) = \sum_i \phi_i(X_p^n) U_i^n \quad (29)$$

where  $\sum_i$  implies a sum over nodes of elements containing  $X_p^n$ .

The particles are moved by a particle-tracking scheme to obtain their temporal up-dated positions. At the end of each time step, the most up-to-date wet and dry regions are identified and the status of all nodes reassigned accordingly, as to whether wet or dry. For elements which are part-wet, the material properties are allowed to adjust over a single element. We do not impose an explicit boundary condition on the surface. This change is directly incorporated into the finite element formulation, since appropriate material properties are assigned to each Gauss quadrature sample points. Therefore, no local re-meshing is required close to the interface. Having assigned the node status and reassigned the material properties, velocity and pressure fields for the new domain are computed at the next time step  $t^{n+1}$ . The velocity,  $U(X_p^{n+1})$ , on free-surface particles for subsequent movement is calculated via:

$$U(X_p)^{n+1} = U(X_p)^n + \sum_i (U_i^{n+1} - U_i^n) \phi_i(X_p^{n+1}) \quad (30)$$

where  $\sum_i$  represents the sum over the nodes of an element containing  $X_p^{n+1}$ . In this manner, particles are shifted to updated positions for the next time step. This procedure is repeated until a stable steady-state is reached.

### 3.2 Wetting/peeling on free surfaces

Specific considerations have been applied to the free-surface, that is itself delineated by a series of particles. In *vertical mixer orientation*, Fig. 2(a), with a concentric/eccentric stirrer arrangement and outer vessel moving, surface wetting ('folding-on of fluid') occurs at the outer vessel and 'peeling-off' occurs at the inner stirrer. For the concentric-stirrer instance, symmetric patterns arise as the flow is a pure shear flow and wetting/peeling apply uniformly about vessel/stirrer. In a *horizontal orientation and at the vessel wall*, peeling may be observed at the advancing surface in contact with the vessel wall; wetting occurs at the retracting surface side (dragging

surface). On the *stirrer*, peeling occurs at both advancing and retarding surfaces fronts, as illustrated in Fig. 2(b).

The stretch (or strain-rate) of free-surface segments is used as a criterion to monitor the extent of wetting and peeling. Stretch is assessed via the ratio of the newly established segment length against its initial length. As such, wetting or peeling is detected if a free-surface segment in contact with a solid boundary is stretched/contracted beyond some specified limiting criteria. This is equivalent to a balance between strain energy and stress. When this situation arises, the free-surface is retarded iteratively, relaxing the newly calculated position, at which the velocity is adjusted accordingly. This automatically relieves the level of stressing. At the same time, governed by restrictions on minimal distance spacing, particle coalescence and vanishing/buckling of free-surface line segments may be guarded against.

In the present work, novel algorithms have been devised to deal with wetting and peeling conditions, between fluid and solid surfaces, represented diagrammatically in Fig. 2(a-b). This provides a schematic illustration for the treatment of fluid-solid body contact points, arising at both outer and inner boundaries in the three-dimensional concentric scenario. In the modeling, particles lying close to the inner and outer boundaries, would move little in the vertical direction, being heavily influenced by the prevailing imposition of no-slip. For example in Fig.2a, consider particle A located at the contact point between the free-surface and the outer vessel-wall. This point is stationary due to no-slip. In contrast, due to centrifugal forces, a neighbour particle B will strive to migrate towards the vessel wall and adhere there. When the angle between the line segment AB and the wall becomes less than  $\theta$  (say,  $20^\circ$ ), particle B is presumed to have attached onto the wall (at B' in Fig.2(a)). This is then recognized as the new contact point for the next time step. In practice, particles A and B are taken to have coalesced at B'. Wetting (or peeling) is also controlled by assessing surface-segment stretch ratio at fluid-boundary contact points (e.g. at A). Stretch adjustment is handled in such a manner as to impact upon control of local stress experienced (relating extent of wetting/peeling to degree and assessment of stretch rate). For example, at and near the inner stirrer, particles migrate away from the stirrer (peel) due to centrifugal forces. Hence, the flow in this region is of a stretching nature. Let us consider two particles close to the inner stirrer-boundary, namely G and H. When the stretch of GH reaches ' $\alpha$ ' (say, 2.0) times its original length, the stationary particle H is relocated at H'. In this manner, the free-surface rolls off (peels from) solid-surfaces. Thus, peeling (or wetting) is detected if a limiting stretch factor ( $\alpha$ ) of a line surface segment nearest the solid boundary is exceeded, according to

$$\frac{\Delta l_i^{n+1}}{\Delta l_i^o} \geq \alpha. \quad (31)$$

The factor ( $\alpha$ ) is taken from empirical estimation and guided by experimental visualization. Here,  $\Delta l_i^o$  and  $\Delta l_i^{n+1}$  represent the length of a segment  $i$  adjacent to a solid boundary at initial time,  $t = 0$ , and new time,  $t^{n+1}$ , respectively.

For both horizontal and vertical orientations with one stirrer, it is found expedient to adopt a limiting value  $\alpha$  of 5.0 at the outer vessel, and 2.0 at the inner stirrer. Further improvements have been made in the horizontal vessel orientation instance (of greater complexity, with advancing/retarding fluid fronts), which demands variation with respect to particular (stirrer) boundary location. Then, dynamic selection of  $\alpha$  is

appropriate to differentiate between inner and outer stirrer-fluid contact points, dependent upon resultant local stressing. Once peeling (or wetting) criteria are satisfied, the position of the free-surface is reassessed, as discussed above, to the relief of stress (or strain) levels. Sub-time steps are introduced to improve field consistency after free-surface movement. Separate time-step control is enforced on surface movement from that for the full wet-domain computation, to reflect the physical problem more closely. Typically, in each Taylor-Galerkin time step, one hundred sub-time steps may be performed.

## 4. Results

Numerical simulations for the above mentioned problems have been conducted at various speeds. The material used for the simulation studies is a model fluid which has shear thinning properties. The results reflect close agreement against equivalent experimental results[20, 21]. This validation exercise has been performed for model fluids, that is, syrup (Newtonian), CMC 1%, CMC(2%), and CMC(3%) for inelastic fluids.

### 4.1 Vertical vessel orientation

For three-dimensional simulations and vertical vessel orientation, a cylindrical vessel with stirrer positions, concentric and eccentric to the axis of the vessel has been considered. For the concentric stirrer instance, free-surface profiles are computed to steady-state for different speeds, namely, 25, 50 and 100 rpm ( $Re = 4, 8, 16$ ), and compared with the equivalent experimental plots. Fig. 3 demonstrates a typical comparison set for 50 rpm ( $Re=8$ ). Since the surface is symmetric, the geometry is sliced through the centre along the axis and the surface positions are plotted in two dimensions. The fluid motion starts from rest with a flat fluid surface. As time progresses, the fluid wets onto the outer wall and peels away from the stirrer, due to prevailing centrifugal forces. Such final steady-state surface profiles are noted to take up a parabolic shape, as expected physically.

The transient rise of the free-surface between experiment and simulation for a typical speed of 100 rpm ( $Re=16$ ) is demonstrated in Fig. 4. In this case, the surface position reaches a steady-state after 1.2 sec. Comparison between steady-states in Figs. 3 and 4, disclose a slight deviation at the higher speed (100 rpm,  $Re=100$ ) between experiment and simulation. This discrepancy may be attributed to the difference in fills and the uniform setting of the wetting-peeling criteria adopted (see below), applied equally across all speeds. We note, that most attention has been paid to matching results at the standard speed of 50 rpm ( $Re=8$ ) of Fig. 3. Free-surface representations in a three-dimensional mode are presented in Fig. 5. These are created by imposing the particle positions obtained from simulation onto a three-dimensional frame. It is observed that as speed increases, the depth of the surface increases, that is, the difference between maximum and minimum levels. Hence, the extent of wetting and peeling rises with increased vessel rotation speed.

Simulations have also been conducted with the stirrer rotating and outer vessel stationary to validate the algorithm and software. In this case, a dip in the free-surface arises in the vicinity of the stirrer, as illustrated in Fig. 6. Once more, this reflects the physical situation accordingly.

Fig. 7 demonstrates local stress and stretch, plotted against time, for a surface line-segment in contact with the stirrer (where peeling occurs). As the distance between particles increases, the stretch increases, until a critical level is reached. This is known as the critical peeling stress. Beyond this phase the fluid peels from the boundary, so that, then the surface line-segment stretch decreases. This procedure equates to a form of energy balance. The local stress follows the same sort of pattern as that associated with the stretch. The match in pattern of stretch and peeling-stress time-trace indicates that either would be equally as valid as monitoring criteria within the algorithm. The flexibility of the techniques employed, in their ability to deal with the most complex of boundary interaction phenomena (would extend equally to slip), highly commends this transient approach.

With eccentric stirrer location, the surface patterns are somewhat more complex than their concentric counterparts. There is rise and fall of the surface position about the stirrer, varying continuously around the stirrer. For comparison between free-surface profiles obtained from simulation and experiment we focus largely upon the eccentric one-stirrer geometry. Since the surface shape is highly complex, exact comparison is difficult and, only qualitative comparison is possible. Plots of surface shape (height) from simulation (speed of 50 rpm,  $Re=8$ ) are illustrated in Fig. 8 and equivalent plots from experimental visualisation are presented in Fig. 9. Figs. 8(a) and (b) illustrate two different orientation views with respect to the vessel, that provide some feel for the surface characteristics, and Fig. 8(c) depicts height contours (perspective view). The maximum and minimum values of height are represented by red and blue colours, respectively. Stirrer position in Fig. 8(c) corresponds to that shown in Fig. 8(a). In the vicinity of the stirrer, there is a dip at the backside of the stirrer, whereas the fluid attempts to climb up the stirrer at the front. On the outer vessel, there is a dip in the front and a rise at the backside of the stirrer, as shown experimentally in Fig. 9(b). Simulations were also performed for the two-stirrer option in likewise mode, reproducing a similar pattern about the second stirrer (see Fig. 8(d))

Fig. 10(a) demonstrates a typical torque-time trace for inelastic fluids from simulation for the eccentric one-stirrer geometry, where torque is an integrated quantity of the rate-of-work done in the whole field. A similar curve is presented in Fig. 10(b) for dough from experimental measurements. Both figures reflect the periodic nature of the torque-time trace. There are different mixing modes identified in the experiments. For comparison purposes, start-up can be ignored, and essentially, it is only the first period, up to 75 seconds, and third period around 100 seconds, where the dough is in contact with stirrer and vessel. At this stage of the modeling, only these periods may be characterised. In the simulations with model fluids, torque levels are halved from the experiments and some similarity may be gleaned out, in periodic rising trend, with those of the experimental mixing periods. Hence, qualitatively, this is held to be a reasonable physical reflection of these process phases.

## 4.2 Horizontal vessel orientation

In this section, we discuss the corresponding scenario, when the vessel is held in a horizontal orientation and the free-surface patterns are obtained by simulation for the two-dimensional ( $r-\theta$ ) orientation of the mixer. Figs. 11(a-f) illustrate the

deformation patterns from the simulations for viscous fluids at 50 rpm, at a quarter of a rotation, two rotations and after twenty rotations of the vessel. Figs. 11(a), (b) and (c) represent simulation results, whereas Figs. 11(d-f) depict results from equivalent experiments. Free-surfaces are observed to move smoothly and approach a steady-state after some twenty rotations of the vessel. Both wetting and peeling phenomena are detected at advancing (forward) and retreating surface fluid-vessel contact points. The effect of wetting is to push more retreating surface segments onto the vessel. Peeling is also identified at the contact point, between the dragging surface and the stirrer. However, for constant  $\alpha$ -factor settings on the stirrer, peeling is not detected at the contact position between the forward advancing surface and the stirrer, because of the relatively low levels of kinematic activity in this particular zone, exacerbated by the asymmetry of the geometry. This is apparent in Fig. 11(a-c). However, according to the experimental pictures (true 3D flow), the fluid does experience peeling in this region, its development is illustrated in Figs. 11(d-f). This is a highly localized feature near the inner stirrer, and as such is difficult to represent accurately in the modelling. For both horizontal and vertical orientation with one stirrer, a limiting value  $\alpha$  of five at the outer vessel is found suitable. For the inner stirrer, different values of  $\alpha$  (line surface segment-solid boundary factor) are applied according to local dictates. For vertical vessel orientation, a static  $\alpha_{\text{stir}}$ -value of two is reasonably acceptable. The horizontal setting has demanded a more dynamic approach, with  $\alpha_{\text{stir}}$ -value varying from 1.3 for the outer stirrer section (narrow gap) to 0.8 for the inner stirrer section (wide gap). The contrast between results for static and dynamic setting of  $\alpha_{\text{stir}}$  is demonstrated in Fig. 12. Particular note should be taken of the centre-vessel surface profile in the image to the right of Fig. 12, generated as a consequence of the dynamic allocation of  $\alpha_{\text{stir}}$ . Here, this adjustment is found absolutely necessary to match closely with the equivalent experimental observations. Again, this complements the flexibility and power of the techniques commended, to identify such fine flow features.

## 5. Conclusions

We have successfully demonstrated the use of a numerical flow solver for non-Newtonian fluids, along with an arbitrary Lagrangian–Eulerian scheme to track free-surfaces in flows within part-filled rotating vessels. Such scenarios are representative of industrial dough kneading processes. We have been able to provide physically realistic simulations for these complex flow problems. Suitable conditions for wetting and peeling are incorporated within the modelling, that provide a close match with the free-surface profiles obtained from counterpart experiments.

In vertical vessel orientation, parabolic surface deformation patterns are obtained for a concentric rotating vessel with a fixed stirrer. Results confirm wetting of fluid, rising at the vessel, and peeling (fall) of fluid at the stirrer. Local stress and stretch values are calculated from stretch-rate and found to be of the same order as the critical stress obtained from the experiments. There is correspondence extracted between simulated and experimentally calibrated results, inclusive of three-dimensional steady-state and transient surface profiles, torque-time traces and scenarios of vessel or stirrer-driven motion. Horizontal vessel orientation presents the more complex wetting-and-peeling circumstance. Here, even the fine detail of wetting and peeling on different boundary sections are faithfully reflected with the implementation of present procedures.

## Acknowledgements

Financial support for this work, from BBSRC (grant no: 58/D08174), RHM Research, United Biscuits, Pilsbury Co., Mono Equipment and Sasib Bakeries, is acknowledged. The support work of Dr. D. Ding, especially within the two-dimensional free surface modelling, is also gratefully acknowledged.

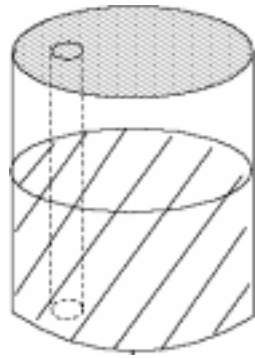
## References

- [1] Wang H.P. and Lee H.S., 1989, "Free and moving boundary problems in C.L.Tucker 111 (ed.), *Fundamentals of Computer modeling for Polymer processing*". Hanser, Munich.
- [2] Harlow F.H. and Welch J.E., 1965, "Numerical calculation of time-dependent viscous incompressible flow of fluid with free-surface". *Phys. Fluids*, 8, pp. 2182-2189.
- [3] Hirt C.W. and Nichols B.D., 1981, "Volume of fluid method for the dynamics of free boundaries". *J. Comput. Phys.*, 39, pp. 201-225.
- [4] Gethin D.T., Lewis R.W. and Tadayon M.R., 1992, "A finite element approach for modeling metal flow and pressurized solidification in the squeeze casting process". *Int. J. Numer. Meth. Eng.*, 35, pp. 939-950.
- [5] Thompson E., 1986, "Use of pseudo-concentration to follow creeping viscous flows during transient analysis". *Int. J. Numer. Meth. Fluids*, 6, pp. 749-761.
- [6] Nassehi V. and Ghoreishy M.H.R., 1997, "Simulation of free surface flow in partially filled internal mixers". *Int. Poly. Process.*, 4, pp. 346-353.
- [7] Hirt C.W., Amsden A.A. and Cook J.L., 1974, "An Arbitrary Lagrangian-Eulerian computing method of all speeds". *J. Comput. Phys.*, 14, pp. 227-253.
- [8] Ramaswamy B., 1990, "Numerical simulation of unsteady viscous free surface flow". *J. Comput. Phys.*, 90, pp. 396-430.
- [9] Sato T. and Richardson S.M., 1994, "Numerical simulation method for viscoelastic flows with free surfaces-fringe element generation method". *Int. J. Num. Meth. Fluids*, 19, pp. 555-574.
- [10] Ding D., Townsend P. and Webster M.F., 1993, "Numerical simulation of filling problems related to injection moulding", *Proceedings of IUTAM symposium on Numerical simulation of non-isothermal flow of viscoelastic liquids*, Netherlands.
- [11] Ding D., Townsend P. and Webster M.F., 1997, "Finite Element Simulation of an Injection Moulding Process". *Int. J. Num. Meth. Heat Fluid Flow*, 7, pp. 751-766.
- [12] Manogg G.J., Townsend P. and Webster M.F., 1997, "Numerical Simulation of Multilayer Injection Moulding". *J. Non-Newt. Fluid Mech.*, 68, pp. 153-167.

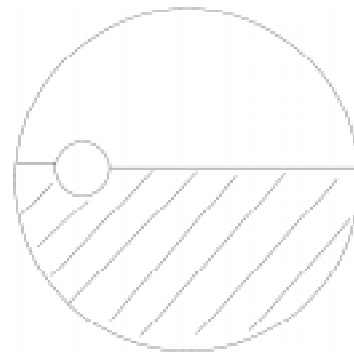
- [13] Ngamaramvaranggul V. and Webster M.F., 2000, "Simulation of Coatings Flows with Slip Effects". *Int. J. Num. Meth. Fluids*, 33, pp. 961-992.
- [14] Ngamaramvaranggul V. and Webster M.F., 2001, "Simulation of Pressure-tooling wire-coating flow with Phan-Thien/Tanner models". *Int. J. Num. Meth. Fluids*, (under review).
- [15] Matallah H., Townsend P. and Webster M.F., 2000, "Viscoelastic Multi-mode Simulations of Wire-coating". *J. Non-Newt. Fluid Mech.*, 90, pp. 217-241.
- [16] Ding D. and Webster M. F., 2000, "Three-dimensional numerical simulation of dough kneading" in Binding D., Hudson N., Mewis J., Piau J.M., Petrie C., Townsend P., Wagner M., Walters K. (Eds.), *X111 Int. Cong. On Rheol., Vol. 2, British Society of Rheology, Cambridge, UK*, pp 318-320.
- [17] Sujatha K.S., Ding D. and Webster M.F., 2001, "Modelling three-dimensional mixing flows in cylindrical-shaped vessels". *ECCOMAS-2001, Swansea, UK*.
- [18] Sujatha K.S. and Webster M.F., 2001, "Modelling three-dimensional rotating flows in cylindrical-shaped vessels". *Int. J. Num. Meth. Fluids* (submitted).
- [19] Couch M.A., Binding D.M., Sujatha K.S. and Webster M.F., 2001, "Experimental and numerical simulation of dough kneading in filled geometries". *J. Food Eng.* (submitted).
- [20] Couch M.A. and Binding D.M., 2000, "Experimental simulation of dough-kneading" in Binding D., Hudson N., Mewis J., Piau J.M., Petrie C., Townsend P., Wagner M., Walters K. (Eds.), *X111 Int. Cong. On Rheol., Vol. 2, British Society of Rheology, Cambridge, UK*, pp 351-353.
- [21] Couch M.A. and Binding D.M., 2001, Private communication.
- [22] Prakash S. and Kokini J.L., 2000, "Estimation and prediction of shear-rate distribution as a model mixer". *J. Food Eng.*, 44, pp. 135-148.
- [23] Hawken D. M., Tamaddon-Jahromi H. R., Townsend P., and Webster M.F., 1990, "A Tayllor-Galerkin-based algorithm for viscous incompressible flow". *Int. J. Num. Meth. Fluids*, 10, pp. 327-351.
- [24] Ding D., Townsend P., and Webster M. F., 1995, "On computations of two and three-dimensional unsteady thermal non-Newtonian flows". *Int. J. Num. Meth. Heat Fluid Flow* , 5, pp. 495-510.
- [25] Matallah H., Townsend P., and Webster M. F., 1998, "Recovery and stress-splitting schemes for viscoelastic flows". *J. Non-Newtonian Fluid Mech.*, 75, pp. 139-166.
- [26] Webster M.F., Ding D. and Sujatha K.S., 2001, "Modelling of free-surface in two and three-dimensions", in: Brebbia C.A. and Sarlen B. (Eds.), *Moving Boundaries-2001, WIT, Lemnos, Greece*, pp. 102-111.

### Figure Legend

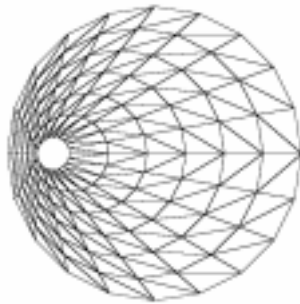
- Figure 1. Meshes: vertical (3D) and horizontal (2D) views; flow domain and surface; (a)-(c), (e) 1 stirrer; (d), (f) 2 stirrers.
- Figure 2. Schematic representation of wetting and peeling : (a) vertical and (b) horizontal ( $r, \theta$ ) orientation.
- Figure 3. Steady-state surface positions,  $Re=8$  (50 rpm); simulation versus experiment.
- Figure 4. Surface positions with time,  $Re = 16$ , (100 rpm); simulation versus experiment.
- Figure 5. Surface patterns: vessel rotating, increasing speed, 3D mode.
- Figure 6. Surface patterns: (a) outer and (b) inner vessel rotation; 3D mode,  $Re = 8$  (50 rpm).
- Figure 7. Variation of stress and stretch with time; peeling from stirrer; 3D,  $Re = 8$  (50 rpm).
- Figure 8. Steady-state free-surface representations (simulation): eccentric, one-stirrer, a-c; two-stirrers, d;  $Re = 8$  (50 rpm).
- Figure 9. Steady-state free-surface profiles (experiment): one-stirrer , two speeds.
- Figure 10. Torque-time trace: a) simulation, b) experiment; 3D,  $Re=8$  (50 rpm).
- Figure 11. Temporal development, surface deformation patterns, horizontal orientation,  $Re = 8$  (50 rpm).
- Figure 12. Steady-state surface patterns, twenty rotations (in time), simulations,  $Re = 8$  (50 rpm): left,  $\alpha_{stir}=2$ ; right,  $\alpha_{stir-outer}=1.3$ ,  $\alpha_{stir-inner}=0.8$ .



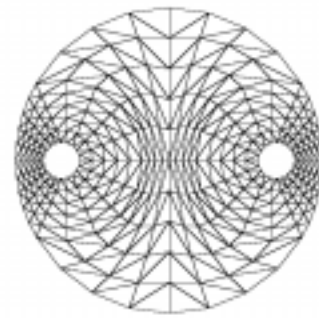
(a)



(b)



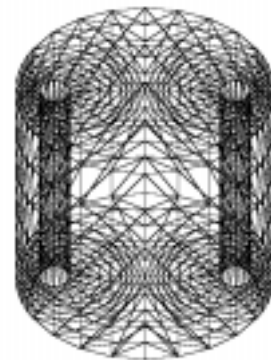
(c)



(d)



(e)



(f)

Figure 1. Meshes: vertical (3D) and horizontal (2D) views; flow domain and surface; (a)-(c), (e) 1 stirrer; (d), (f) 2 stirrers.

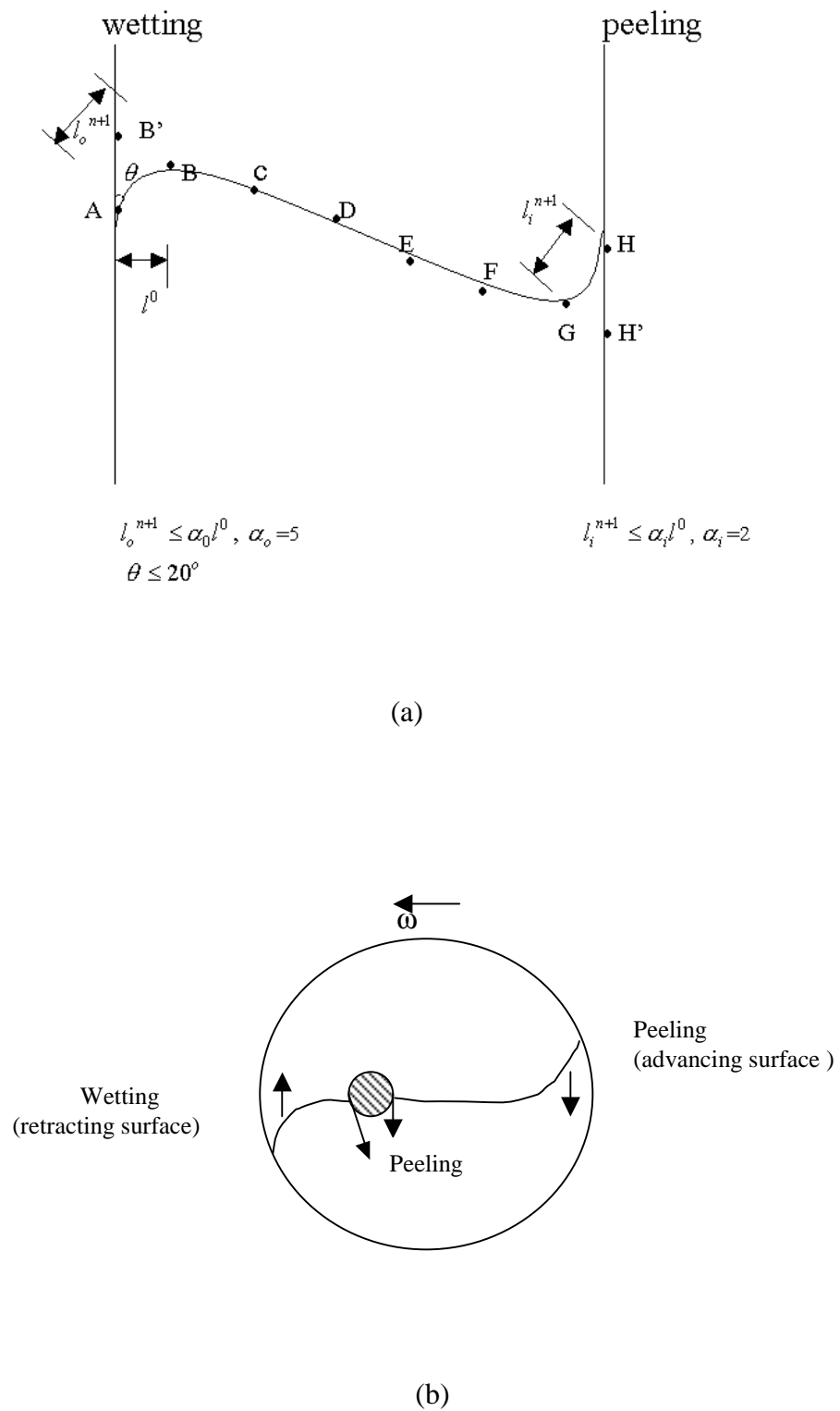


Figure 2. Schematic representation of wetting and peeling:  
 (a) vertical orientation; (b) horizontal ( $r, \theta$ ) orientation.

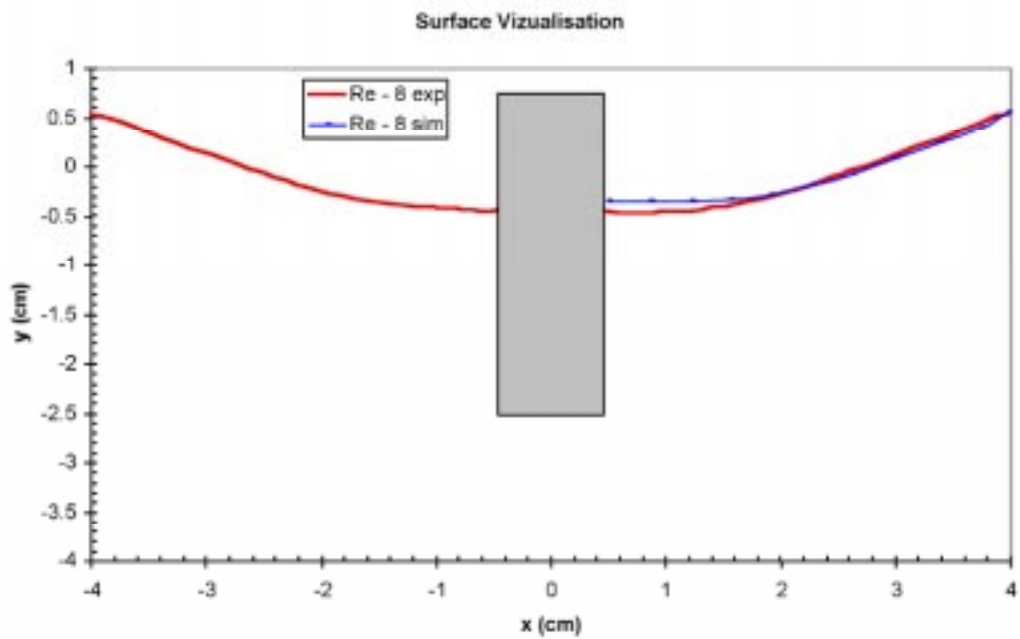


Figure 3. Steady-state surface positions,  $Re=8$  (50 rpm); simulation versus experiment.

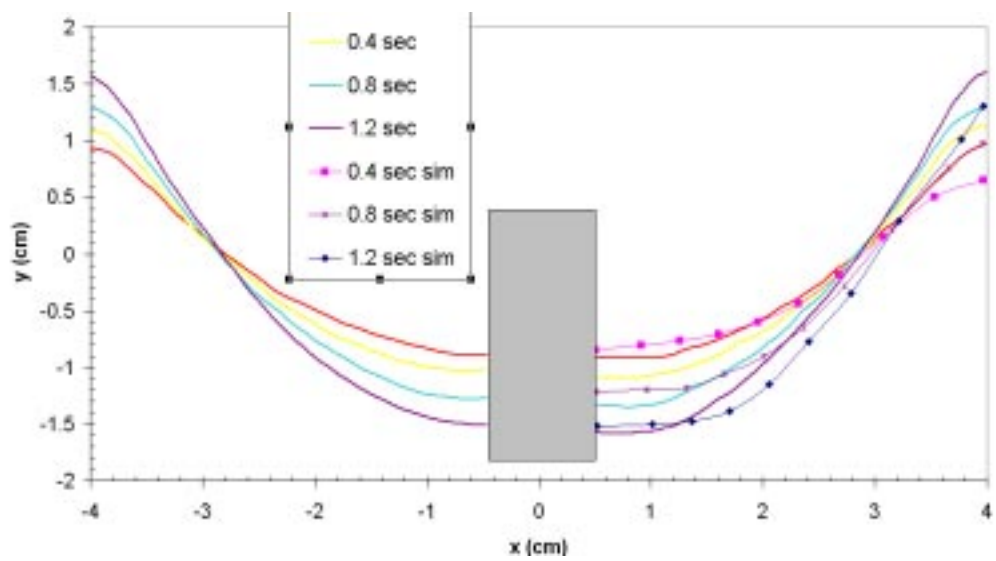


Figure 4. Surface positions with time,  $Re = 16$ , (100 rpm); simulation versus experiment.

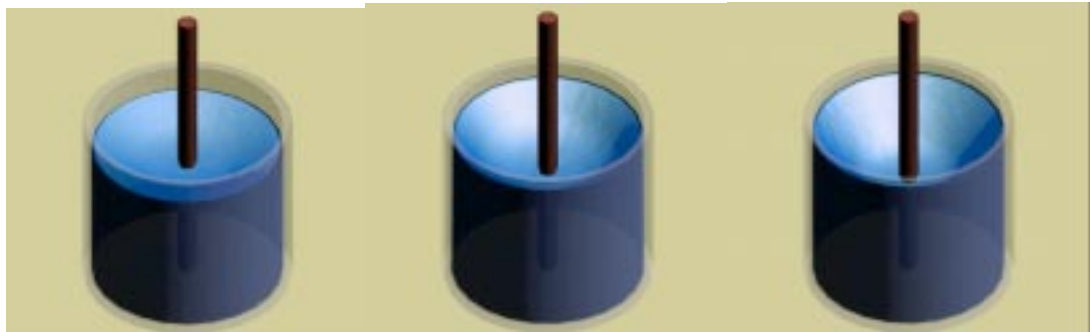
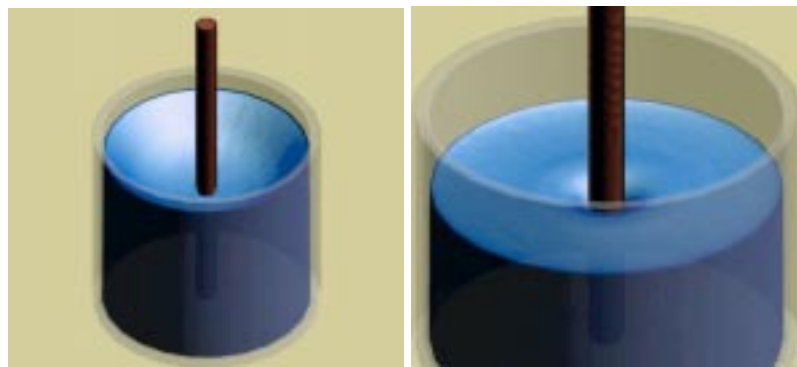
(a)  $Re = 4$  (25 rpm)(b)  $Re = 8$  (50 rpm)(c)  $Re = 16$  (100 rpm)

Figure 5. Surface patterns: vessel rotating, increasing speed, 3D mode.



(a)

(b)

Figure 6. Surface patterns: (a) outer and (b) inner vessel rotation; 3D mode,  $Re = 8$  (50 rpm).

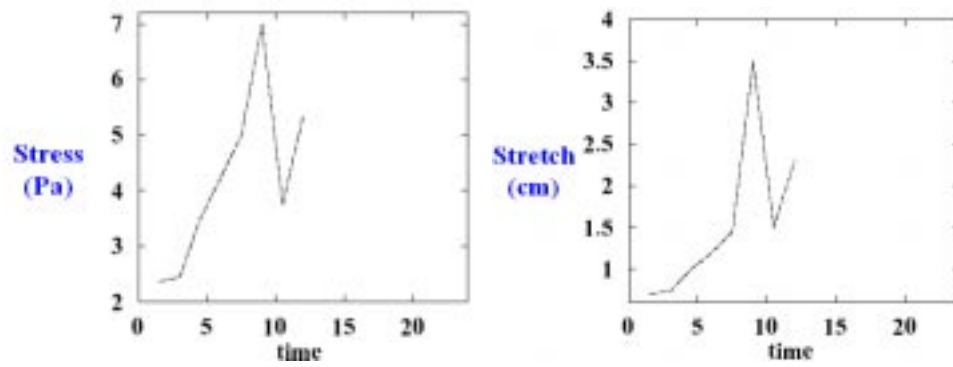


Figure 7. Variation of stress and stretch with time; peeling from stirrer; 3D,  $Re = 8$  (50 rpm).

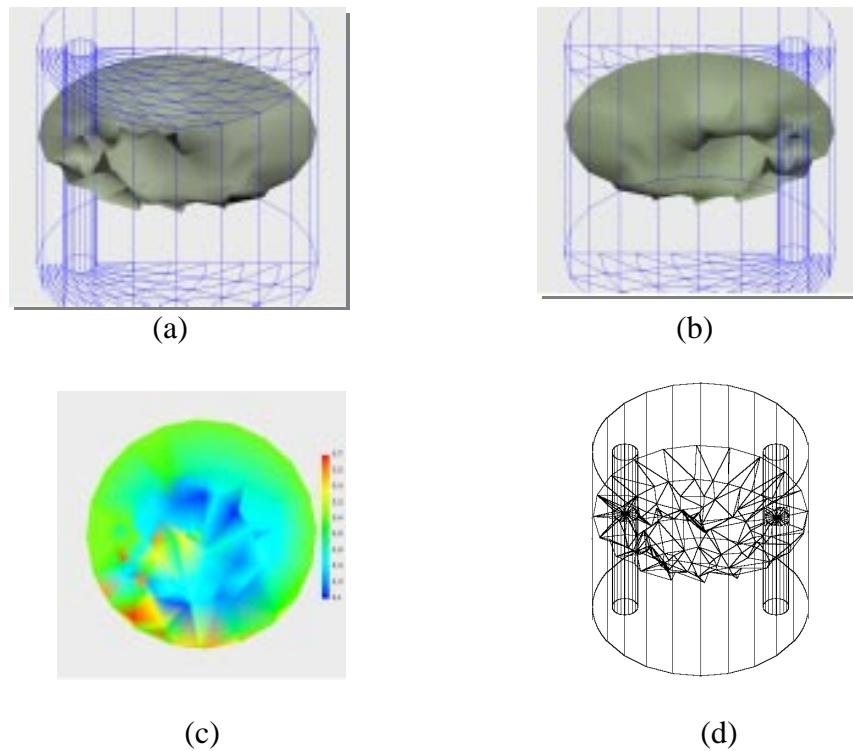


Figure 8. Steady-state free-surface representations (simulation): eccentric, one-stirrer, a-c; two-stirrers, d;  $Re = 8$  (50 rpm).

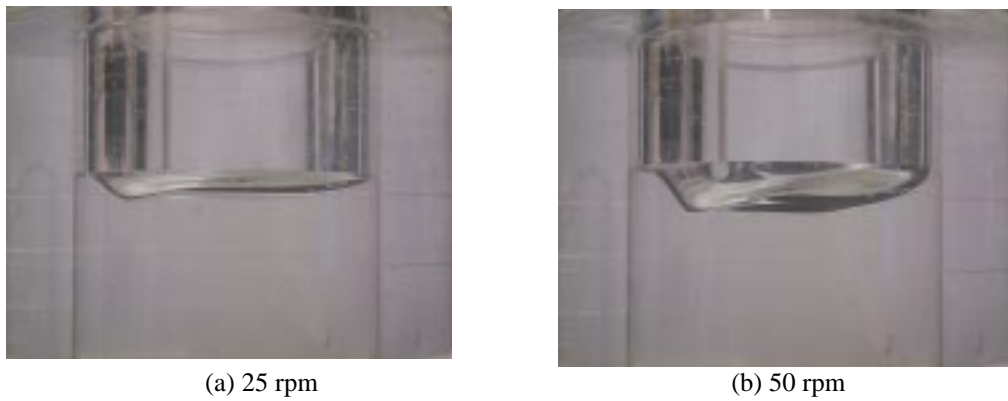
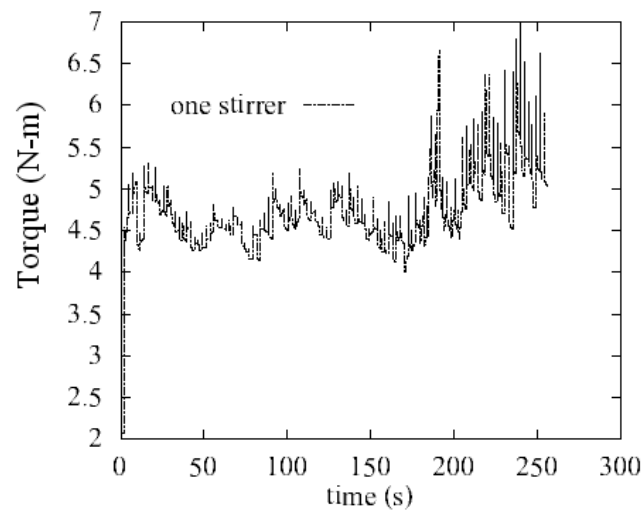
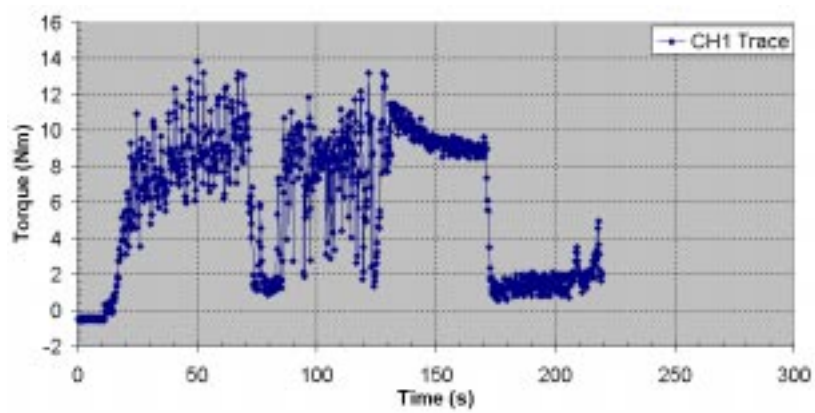


Figure 9. Steady-state free-surface profiles (experiment): one-stirrer , two speeds.



(a)



(b)

Figure 10. Torque-time trace: a) simulation, b) experiment; 3D,  $Re=8$  (50 rpm).

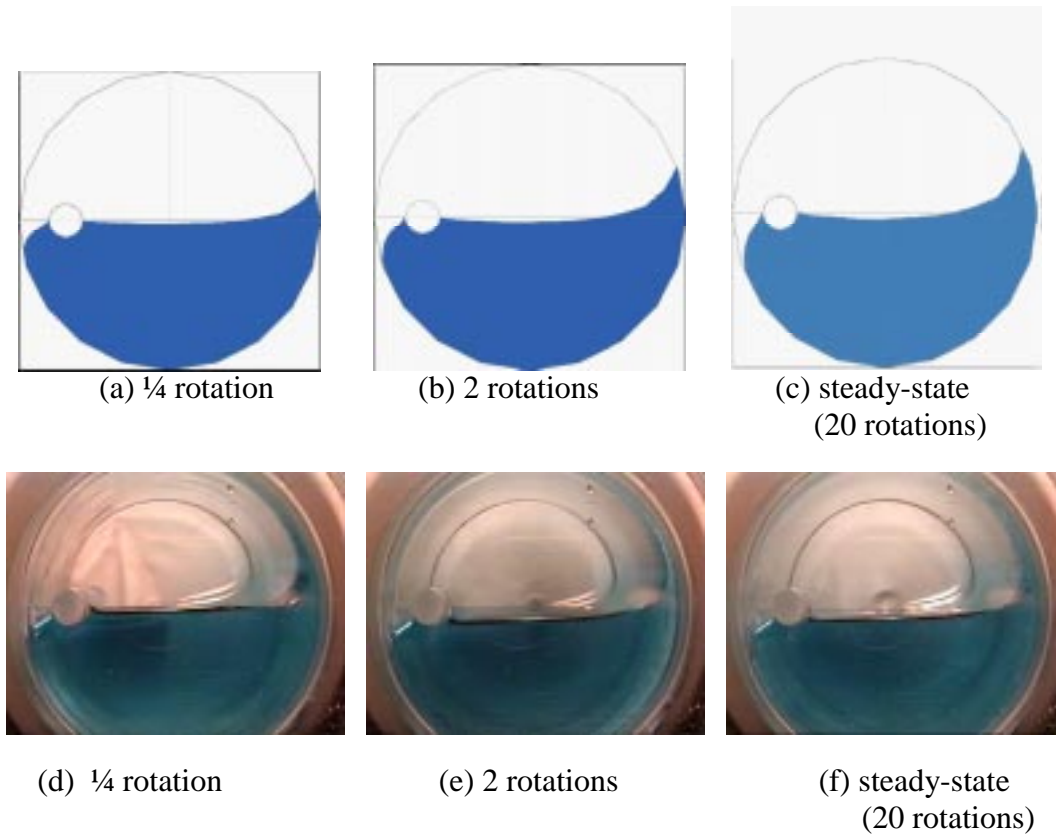


Figure 11. Temporal development, surface deformation patterns, horizontal orientation,  $Re = 8$  (50 rpm).



Figure 12. Steady-state surface patterns, twenty rotations (in time), simulations,  $Re = 8$  (50 rpm):  
left,  $\alpha_{\text{stir}}=2$ ; right,  $\alpha_{\text{stir-outer}}=1.3$ ,  $\alpha_{\text{stir-inner}}=0.8$ .

